

Three-dimensional simulations of NIF implosions: insight into experimental observables

Brian K. Spears,^{1, a)} David H. Munro,¹ Scott Sepke,¹ Joseph Caggiano,¹ Dan Clark,¹ Robert Hatarik,¹ Andrea Kritchler,¹ Dan Sayre,¹ Charles Yeamans,¹ Jim Knauer,² Terry Hilsabeck,³ and Joe Kilkenny³

¹⁾*Lawrence Livermore National Laboratory, P.O. Box 808, Livermore, California 94551-0808, USA*

²⁾*Laboratory for Laser Energetics, 250 E. River Road Rochester, New York 14623-1212, USA*

³⁾*General Atomics, P.O. Box 85608, San Diego, California 92186-5608, USA*

We simulate in 3D both the hydrodynamics and, simultaneously, the X-ray and neutron diagnostic signatures of National Ignition Facility (NIF) implosions. We apply asymmetric radiation drive to study the impact of low mode asymmetry on diagnostic observables. We examine X-ray and neutron images as well as neutron spectra for these perturbed implosions. The X-ray images show hot spot evolution on small length scales and short time scales, reflecting the incomplete stagnation seen in the simulation. The neutron images show surprising differences from the X-ray images. The neutron spectra provide additional measures of implosion asymmetry. Flow in the hot spot alters the neutron spectral peak, namely the peak location and width. The changes in the width lead to a variation in the apparent temperature with viewing angle that signal underlying hot spot asymmetry. We compare our new expectations based on the simulated data with NIF data. We find that some recent cryogenic layered experiments show appreciable temperature anisotropy indicating residual flow in the hot spot. We also find some trends in the data that are at odds with our simulation and theoretical understanding.

I. INTRODUCTION

Implosion experiments in the inertial confinement fusion (ICF) program at the National Ignition Facility (NIF) aim to produce thermonuclear fusion by assembling a spherically symmetric hot spot surrounded by cold, dense deuterium-tritium (DT) fuel⁸. Experiments to develop an igniting platform have entered the alpha-heating regime by producing more than twice as much neutron yield as an equivalent implosion not self-heated by alpha particles^{10,11}. However, the current performance is likely limited by asymmetry in the implosion leading to incomplete stagnation and residual flow in the hot spot throughout the fusion burn process.

Here we investigate the experimental signatures of implosion asymmetry. We do this by simulating in 3D an ICF experiment. The simulation includes detailed radiation transport and hydrodynamics done by HYDRA¹⁶. In addition, we simulate a large set of diagnostics and the experimental signatures they record – X-ray images, neutron images, and neutron spectra, among others.

We find that shape distortions in the implosion may be seen differently by X-ray and neutron cameras. Furthermore, X-ray images themselves may appear very similar across observed X-ray energy bands. Our simulated neutron spectra show angular dependence of neutron peak centroid shift and neutron peak width as predicted by recent theoretical work^{2,17}. The fluid velocity distribution in a non-stagnated implosion increases the neutron peak width, which may be misinterpreted as an increase in ion temperature⁴. We point out that variation with viewing

angle of the neutron peak width, caused by angular variation in the fluid velocity, is a nuclear-based measure of implosion asymmetry complementary to X-ray imaging.

Equipped with expectations based on our simulated diagnostics, we turn to the database of results from recent high-foot implosions on NIF for comparison. The examination reveals that nuclear signatures of asymmetry are present in the NIF database. These asymmetries range from very small to quite substantial. In the most asymmetric cases, we find a correspondence between X-ray image distortion and nuclear asymmetry signatures. We also find some trends that are not consistent with simulation-based expectations. Here we point to the angular variation of neutron peak width as seen in both DT and DD neutrons where the relationship between the two signatures differs in experiment from that seen in 3D simulation.

II. SIMULATION OF 3D IMPLOSIONS WITH LOW-MODE ASYMMETRY

A. Numerical methodology

We begin our investigation of asymmetries with 3D radhydro simulations of a high foot implosion⁶. These high adiabat implosions show low instability growth at the ablation front. Thus perturbations communicated to the hot spot by low-mode-asymmetric radiation drive dominate. The ICF program has focused in the past on correcting small drive perturbations based on detailed 2D modeling¹⁵. However, experimental X-ray images from NIF implosions show that hot spot shape, inferred from x-ray self-emission¹⁴, are neither spher-

^{a)}Electronic mail: spears9@llnl.gov

ical nor axisymmetric¹⁸. Decomposing the hot spot into spherical harmonics ($Y_{l,m}$), we find contributions for $l, m \leq 4$. Consequently, we focus on simulations supporting asymmetric perturbations with this frequency content.

Our radhydro simulation proceeds in two phases. First, we initiate the problem on a spherical polar mesh and define the asymmetric radiation drive. The radiation flux driving the capsule has angular asymmetry described by a spectrum of l and m numbers. The magnitude of the components is also time-dependent. In particular we chose to apply dynamically varying $Y_{2,0}$ and $Y_{4,0}$ consistent with post-shot investigations of high-foot experiments¹³. To make the radiation asymmetry fully 3D, we apply a mode 1 perturbation, $Y_{1,-1} = Y_{1,0} = Y_{1,1} = 0.03 * Y_{0,0}$ exclusively in the high-flux peak of the radiation drive. Previous work¹⁹ shows that this type of perturbation produces asymmetry in both X-ray and nuclear diagnostic signatures at clearly detectable levels. To resolve asymmetries of these wavelengths in the early implosion phase, from the initial shell radius of about 1000 μm to an imploded shell radius of about 250 μm , we require only modest angular resolution of 128 mesh lines in both angular directions. This is substantially lower resolution than the extremely detailed simulations described by Clark et al.⁵. This lower resolution frees up computational resources, the most precious of which is system memory, to do detailed Monte Carlo simulations of thermonuclear burn processes, discussed in more detail later.

Once the dense shell has imploded to 250 μm , the asymmetric radiation drive produces high-speed flows through the nascent central hot spot. The singular origin in the spherical polar mesh and the large aspect ratio zones surrounding it poorly resolve the lateral flows in the imploded core. This motivates us to remap the problem to a multi-block box mesh. This mesh replaces the singular origin point with a logically Cartesian box. Additional blocks are connected to the central box faces and to each other, producing 7 connected boxes that cover the problem. The remap not only produces a topology that better handles the flow, but also allows high resolution to be focused on the forming hot spot where we resolve flows on the 10- μm length scale. The simulation runs through stagnation, peak neutron production, and later decompression on this mesh topology.

B. Description of the implosion

The 3D asymmetric radiation drive produces strong flows that disrupt and perturb the hot spot. The 1 keV isosurface can be thought of as the boundary of this hot spot. In Figure 1, we show the evolution of the hot spot boundary from $t=-100\text{ps}$ to peak neutron production at $t=0\text{ps}$. The hohlraum axis is vertical here. In frames (a) - (c), the mode 2 and mode 4 dynamic asymmetry has produced oscillations in the hot spot boundary at

modes 2 and 4. Namely, the hot spot is swinging from prolate back through spherical, and similarly for mode 4. The mode 1 asymmetry results in a radiation drive imbalance – high drive at the top right and low drive at the bottom left. This imbalance produces a mode-1-induced jet¹⁹ forming in (c), but evolving until it has crossed the entire hot spot by bang time in (f). This jet feature is a hallmark to be tracked in later analysis of the simulated diagnostics.

We find additional insight by examining the hot spot from a variety of angles at a fixed time, neutron bang time, in Figure 2. There are two features of primary interest. First, the mode-1 jet has fully penetrated the hot spot, leaving a substantial hole, most visible in frames (b), (c), or (d). We will show in Sec. III that such a 3D feature is visible in X-ray images only with high resolution. The second feature of interest is the higher-mode content in the hot spot shape. Flows on the 10- μm length scale develop throughout the stagnation phase and are seeded wholly by the low-mode drive perturbation.

This degradation of the hot spot has substantial impact on implosion performance²⁰. Table I(comparison of 1D, 3D performance plus table). note in 3D: reduced yield/pressure, reduced Tion, increased apparent Tion (see diags later), early bang time.

	1D	3D
Yield [neutrons]	1.1e15	3.3e14
Average Thermal T_{ion} [keV]	2.4	2.2
Apparent T_{ion} [keV]	2.4	3.2
Bang time [ns]	16.64	16.54
Peak pressure [Gbar]	173	60

TABLE I.

III. DETAILED SIMULATED DIAGNOSTIC OUTPUT

We put special emphasis on simulating in detail the diagnostic signatures measured by NIF instruments. These signatures, produced by both neutrons and x-rays, provide our view into the experimental implosions. Ultimately, our understanding of the experiment rests on our expectations about these signatures. Our principal goal is to better understand the effects that large, 3D asymmetries have on the diagnostic observables and what these signatures can tell us about the asymmetry and quality of our implosion. We have arrived at some new expectations and hypotheses about data based on our diagnostic simulations, and we describe those here.

For the first time, we can simultaneously simulate low-resolution hydrodynamics and detailed neutron and X-ray production in three dimensions. We discuss Monte Carlo neutronics first, where managing computational resources is critical. HYDRA transports neutrons, gamma rays, and light ions (hydrogen and helium isotopes) produced during burn. We account for elastic and inelastic

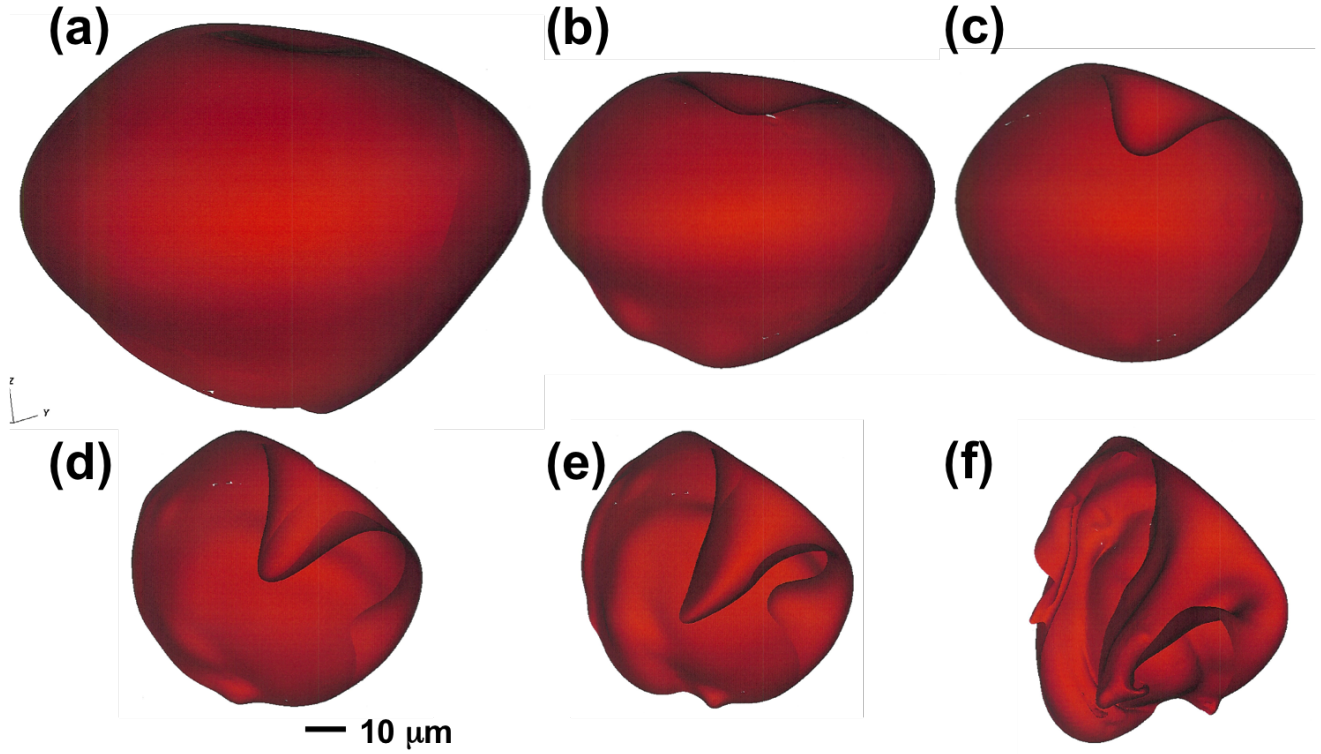


FIG. 1. cut-away of simulated hot spot boundary. We take the 1 keV ion temperature isosurface as the hot spot boundary. We have shown it here at several times approaching peak neutron production. The hot spot evolves from 100 ps before peak neutron production (panel (a)) until the time of peak production (panel (f)). The time-dependent asymmetry produces oscillations in the hot spot shape and drives a strong jet that penetrates the hot spot from the top right.

collisions, including in-flight reactions of daughter particles, Doppler shifts, and relativistic kinematics. Charged particles, in particular alpha particles, slow down and heat the simulated plasma, including recoils from neutron collisions. We tally important quantities to build simulated diagnostics. For example, when a neutron escapes the simulation, we tally its speed and direction to build the energy spectrum of escaping neutrons.

However, too few of these transport Monte Carlo particles happen to escape in the direction of some diagnostic instrument (such as a neutron imager or neutron time-of-flight spectrometer), to build an image or spectrum accurate enough to compare to real data. Hence, along a few specific lines of sight, we track a population of diagnostic neutrons (for example), all moving in a single direction toward some detector, which do not contribute back to the hydrodynamic simulation like the transport particles. These diagnostic particles solve the adjoint problem⁷, and therefore need not be fully tracked like the transport particles. Each nuclear event (e.g.- TN reaction or collision) among the transport particles launches some number of diagnostic neutrons directly toward the desired detector, carrying a weight equal to the number of neutrons per steradian moving in that direction, and with energy according to the distribution, the event would produce. We track this diagnostic neutron

along its straight line path, decrementing its weight by the probability that it would scatter or be absorbed by further Monte Carlo nuclear events as it flies out of the plasma, then tally the number of neutrons per steradian it represents on exit, along with its energy and trajectory. Since their weight is infinitesimal (neutrons per steradian), diagnostic neutrons have no effect on the plasma and produce no additional Monte Carlo particles to track. Despite the huge improvement in statistics for building a diagnostic signal, we still consume all of the memory on our computer, 16*64 GB of RAM, to hold these diagnostic particles together with the transport particles and plasma simulation.

We transport X-rays by multigroup diffusion in the HYDRA simulation, since Monte Carlo radiation transport would be too expensive. But we simulate X-ray images by straightforward three dimensional ray tracing: To simulate a given camera, we construct a square grid of parallel rays, one ray per image pixel, each ray directed toward the diagnostic. The 300 um/ps speed of X-rays is practically infinite, and at core imaging energies, X-ray refraction is negligible. Thus at each instant of time, we simply integrate the transport equation on each ray as it passes through the hexahedral HYDRA mesh. For the ray trace, we augment the LTE absorption opacity we use for transport by the (Thompson) scattering pro-

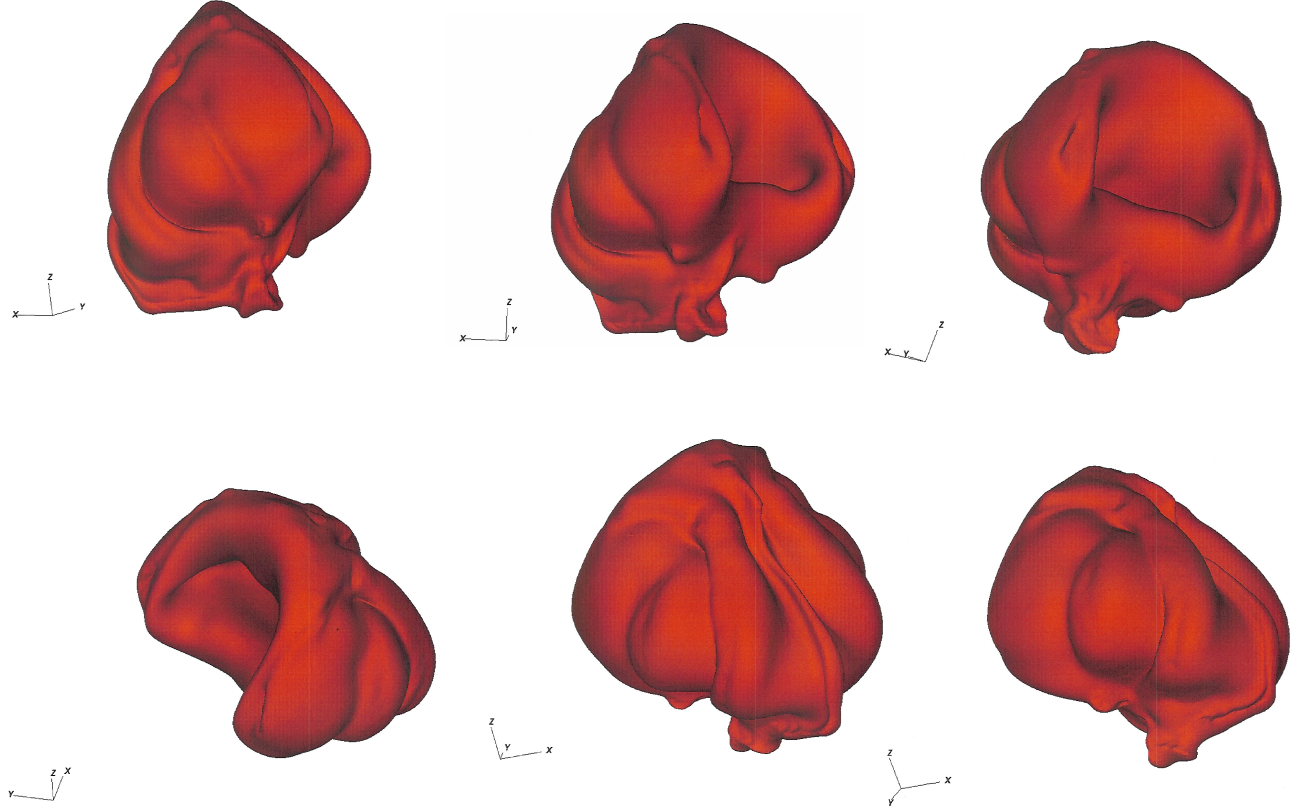


FIG. 2. hot spot viewed from different angles. We show here the hot spot boundary (1 keV isosurface) at peak neutron production. The panels show the hot spot as viewed from multiple directions. We note the small scale length structure that develops and also highlight the hole that has been punched in the hot spot by the jet

portional to the free electron density. We augment the LTE emissivity by a corresponding amount proportional to both electron density and radiation density, so that the augmented opacity accounts for scattering out of the ray, while the augmented emissivity accounts for scattering into the ray. This in-scatter is isotropic, consistent with the diffusive radiation transport, with similar failure to represent the directionality of the radiation field. For each ray, we compute the sequence of cells and the length of the ray segment inside each cell. Assuming each cell is a uniform emitter and absorber with its augmented emissivity and opacity, we compute the attenuation and self-emission produced by each segment. Finally, we accumulate the self-emission, that is, power per unit area per steradian in each photon energy group, with each cell in the sequence attenuating what enters and contributing its own self-emission. The total emission from the final cell in the sequence is the contribution of that ray to the image at that time. We sum over photon energy and integrate over time according to the spectral response and temporal gating function, respectively, of the instrument we are simulating in order to produce a final image.

A. Simulated X-ray and neutron images

We now examine simulated X-ray image sequences (movies) to better understand the detailed evolution of the hot spot. We show in Figure 3 the 9 keV x-ray emission at multiple spatial resolutions and several times before and at peak neutron production. The images show several key features. First, the mode-1 induced jet visibly dims the hot spot during its transit (compare Figure 1 panel (e) and Figure 3 at -90 ps). This feature is a hallmark of the mode-1 radiation imbalance responsible for much of the degradation from 1D performance. Yet, it requires at least $10 \mu\text{m}$ resolution to identify this feature in the images. Also notable is the short-scale-length structure visible in the $1-\mu\text{m}$ resolution images. Similar structure was noted in Figure 2. In the x-ray images, emission from Si-doped CH ablator material mixed in the initial DT gas emphasizes these fine-scale flows. Again, this structure is lost by $20-\mu\text{m}$ resolution. We finally highlight dynamic evolution across frames. The time-dependent drive asymmetry has produced hot spot flows that evolve substantially on the 30-ps time scale. These observations from simulated images suggest that we should expect rapid, fine scale evolution in x-ray self emission images, and they have supported the develop-

ment of a high-performance x-ray camera capable of 10 μm spatial and 10 ps temporal resolution. This camera, known as DIXI, has been successfully deployed on NIF experiments beginning with a DT-layered implosion N140819. The data confirm dynamic evolution with characteristic scales similar to those reported here [cite Sabrina].

We have also compared x-ray images filtered for a variety of x-ray energy bands, namely 9, 12, 16, and 20 keV (see Figure 4). To our surprise, the image topography is very similar. Conventional expectations suggest that the relatively stronger attenuation of 9 keV x-rays by cool CH ablator material would alter the hot spot emission images. Higher-energy 20 keV x-rays would be expected to more effectively escape the ablator, emphasizing the hottest parts of the hot spot. In fact, the brightness of the images is reduced with energy as expected. However, image shapes are nearly unchanged across energies. Thus, the ablator material, in the simulations, effectively acts as an intensity filter without affecting spatial gradients across energies.

We find additional insight by comparing x-ray images to primary neutron images in Figure 5. The primary neutron images are filtered to accept mostly unscattered neutrons from a 13 to 15 MeV band centered at the (approximately) 14 MeV DT neutron birth energy. Thus the primary neutron images provide an alternative view of the hot spot. Again, conventional expectations are that the x-ray and neutron images reflect process that scale in grossly the same way with temperature and density. Consequently, they might be expected to be very similar. However, we find key differences in the images. Though the physics of the image production is complicated, we believe two mechanisms are the chief sources of the discrepancies. First, the emissivity of neutrons increases less strongly with temperature than does the emissivity of x-rays. This drives x-rays to emphasize temperature gradients more strongly than do neutrons. Differences in temperature histories of both electrons and ions are also a source of discrepancy. The X-ray production peaks more than 50 ps before the neutron production. During the first half of the x-ray production, the ion temperature, which drives neutron production, is higher than the electron temperature, which drives x-ray production. This means that X-ray and neutron signals are weighting different times of the implosions as well. Together, the dissimilar emissivities and histories mean that the two production processes can emphasize different times and spatial locations in the hot spot. Viewed this way, it is less surprising that the lobed neutron image in Figure 5 displays a bright bottom left lobe and a dim top right lobe compared to the more uniform X-ray image. Nevertheless, it is exceedingly difficult to probe the 3D simulation in space and time to determine the exact physical sequencing and sensitivities that lead to the particular image differences shown.

B. Simulated neutron spectra

Neutron spectra, as compared to images, are amenable to very detailed analysis coupling the fluid state, thermodynamics and fluid dynamics, with the neutron production. Analysis of the spectra gives multiple features that reflect the state of the emitting plasma. These include the location (in neutron energy or neutron velocity) of the primary peak of the spectrum and the width of this peak (see Figure 6). Detailed theory shows that these features encode the hot spot's thermal temperature, its bulk translation, and its internal, residual flow.

The spectra are measured in experiments by neutron time-of-flight (nTOF) detectors¹. As neutrons propagate from the hot spot to the nTOF located about 20 m away, the neutrons disperse based on energy – the most energetic particles arriving before those with less energy. The spectral resolution results from the temporal resolution of arrival time at the detector.

Let us first examine the physical processes that shift the centroid of the primary peak. At its simplest, the peak is located near the birth energy of DT neutrons. The most obvious shift occurs due to rigid or bulk translation of the neutron emitting fluid. Heuristically, we can think that the neutron arrival encodes the neutron birth velocity and the fluid velocity as $t_a = d/(v_0 + v_{fluid})$, where v_0 is the birth velocity of DT neutrons, d is the distance to the detector, and v_{fluid} is the translational velocity of a fluid element or a continuum undergoing rigid translation. There is, in addition to this fluid mechanical effect, a thermal contribution to the peak shift³. Thermal velocities of particles are carried into the collision between reactants, here D and T. The kinetic energy of these particles, relative to the center-of-mass frame of the collision, promotes the energy that a neutron carries after the reaction. We can account for these effects simultaneously by writing the emitted neutron energy in terms of the energy released by DT reactions, the reactant center-of-mass velocity, and the reactant kinetic energy. Following [ref Munro], we write

$$E_n = \frac{m_\alpha + Q/2}{m_D + m_T} Q + \mathbf{p}_n \cdot \mathbf{v}_{cm} + \frac{m_\alpha + Q}{m_D + m_T} K \quad (1)$$

where m_α , m_D , and m_T are the alpha, deuteron, and triton masses. Q is the energy liberated in a DT reaction, K is the center-of-mass kinetic energy of the reactants, \mathbf{p}_n is the neutron momentum, and \mathbf{v}_{cm} is the velocity of the center of mass of the reactant pair. The first term in equation 1 represents the neutron birth energy of a reacting DT pair colliding with negligible relative velocity, or 14.028 MeV. The second term, typically about 30 times smaller in NIF ICF implosions, represents the peak shift due to bulk motion. The last term, another factor of 30 smaller than the second, represents the shift in the peak due to particle kinetic energy, or for a fluid continuum, the thermal temperature.

At NIF, a nearly-orthogonal triad of nTOF detectors

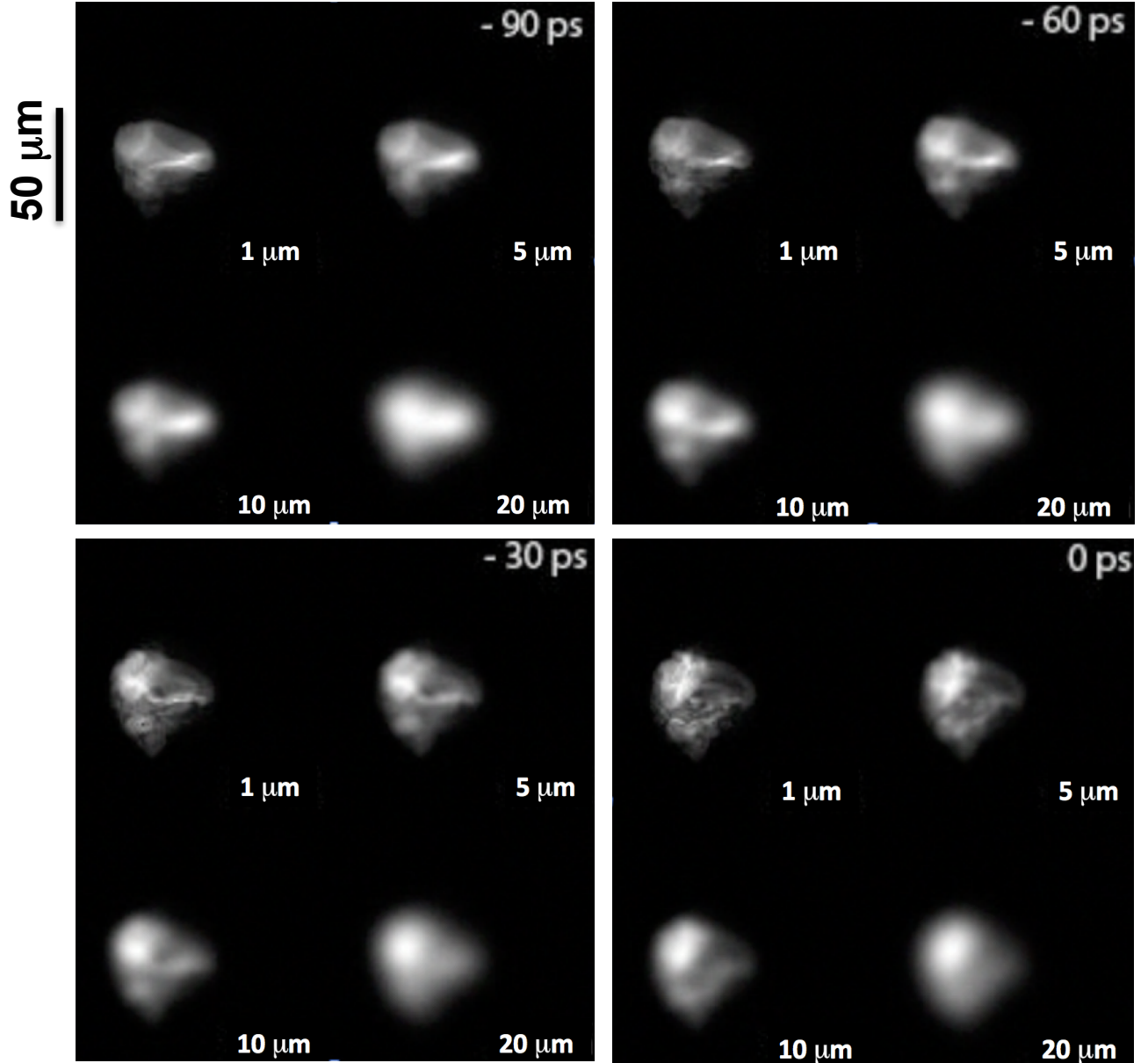


FIG. 3. simulated X-ray images with high temporal and spatial resolution. We show simulated 9 keV X-ray images at four times: -90 ps, -60 ps, -30 ps and 0 ps, where 0 ps is the time of peak neutron yield. Each time shows four resolutions: 1 μm , 5 μm , 10 μm , and 20 μm . The fine scale features, jet, and rapid evolution discussed in figures Figure 1 and Figure 2 are clearly visible at 1 μm resolution. By 20 μm , the features are difficult to identify.

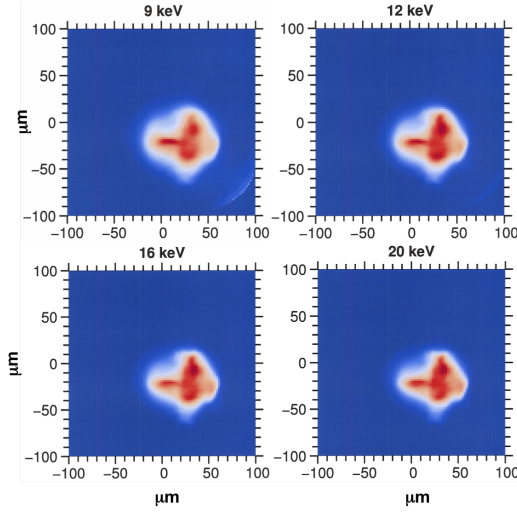


FIG. 4. X-ray images at multiple energies. Simulated X-ray images at 9 keV, 12 keV, 16 keV, and 20 keV show little difference in appearance across energies, though the total signal falls as expected.

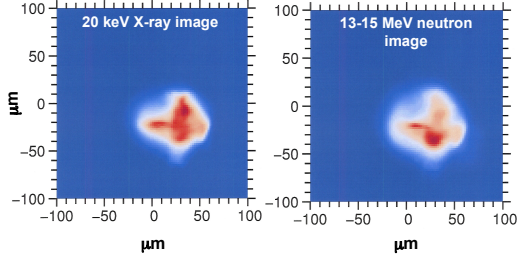


FIG. 5. hard X-ray and primary neutron images. Time-integrated X-ray and neutron images are different. Differences in temperature sensitivity of emissivity for the X-rays and neutrons provide a partial explanation. Differences in electron and ion temperature histories also lead to disparities.

measures the peak shift on three lines of sight. The thermal shift is estimated using measurements of the ion temperature, discussed further below. Thus, the non-thermal shift can be used as a measure the *neutron-averaged* bulk velocity along an instrument line of sight. The triad of measurements gives the resultant vector associated with the center-of-mass or bulk motion of the entire burning hot spot. At NIF, these velocities have been observed to range from nearly zero up to 160 km/s with a precision of less than 30 km/s. Simulations show that these velocities are damaging to implosions, with 100 km/s velocities resulting in halving of the neutron yield¹⁹.

The thermal state and the underlying fluid flow also affect the peak width, with both process affecting the observation more equally than in the shift case. The width is fundamentally set by Doppler broadening due to the Maxwellian distribution of ion velocities in the emitting fluid. However, the peak is additionally broadened by the variance of the fluid velocity field. We emphasize strongly

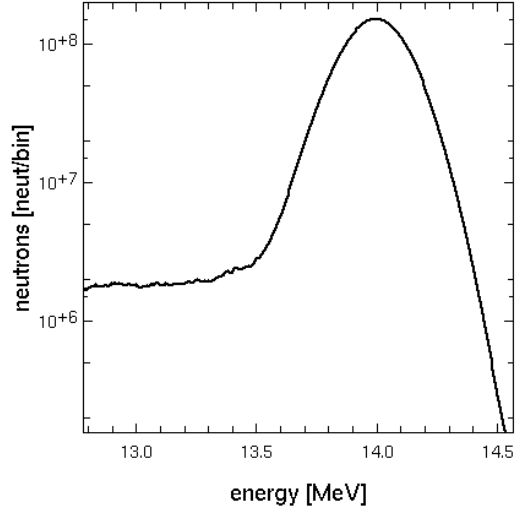


FIG. 6. simulated DT neutron spectrum. Monte Carlo neutron transport in HYDRA produces detailed neutron spectra. DT neutron spectra show a thermally- and flow-broadened peak centered near 14 MeV. Neutrons scattered by cold DT are also visible here in the band below 13.5 MeV. We compute similar detailed spectra on five diagnostic lines of sight. We compute less resolved spectra at 1600 locations uniformly distributed on the sphere.

that the rigid-body translation or resultant bulk velocity that affects the peak location does *not* alter the width. Instead, the *spread* in fluid velocities broadens the peak. We keep with the early work by Brysk and associate a temperature with the neutron peak width. Here, we will call this apparent temperature the Brysk temperature, or T_{Brysk} . We follow¹⁷ and write the apparent temperature as

$$T_{Brysk} = T_{thermal} + \left(\frac{m_D + m_T}{k} \right) \sigma_v^2 \quad (2)$$

$T_{thermal}$ is the thermodynamic temperature that characterizes the Maxwellian distribution of ion thermal velocities and k is Boltzmann's constant. The σ_v^2 is the variance of the emitting plasma velocity field taken along the line of sight of a detector. We can see that the fluid variance raises the apparent temperature. Any fluid flow process that increases velocity variance – rotation, shear, swirling, turbulence, or simply higher spherical implosion velocity – will increase the apparent temperature.

We now examine our 3D simulation to illustrate the connection between the thermodynamic temperature and the flow field as they contribute to the neutron spectral peak properties, location and width. We first consider a two-dimensional histogram of neutron production along a single line of sight (Figure 7, line of sight 1, or LOS 1). We have counted the number of neutrons produced at a given thermal temperature (T) and at a given velocity (u) along the line of sight. That is, we build the histogram in (T, u) -space. This histogram is both temporally and

spatially integrated. We have removed production time and length-scales from the problem and discussion.

The LOS 1 (T, u) distribution in Figure 7 gives the spectrum labeled LOS 1 in Figure 8. The spectral peak is shifted slightly by thermal motion, but greatly by the more than 100 km/s neutron-averaged velocity (indicated by the central blue tic on the velocity axis). The neutron-averaged velocity does not affect the width.

The velocity variance, σ_v^2 , however, increases the width substantially beyond the purely thermal broadening (we have indicated the velocity variance by the leftmost and rightmost blue tics on the velocity axis). To further clarify the relationship between thermal temperature and flow, we compare the spectrum produced by the (T, u) distribution along LOS 1 (shown in black in Figure 8) with the spectrum produced by a plasma in the localized state denoted by the blue point in Figure 7 on LOS 1. The localized state has a neutron-averaged velocity equal to that of the distributed plasma, by crucially, it has no flow variance. Further, the localized plasma has a thermal temperature of 4 keV. In fact, the spectrum associated with the gray distribution and that associated with the blue point are experimentally indistinguishable. Specifically, they have identical peak widths and peak locations. Thus, a plasma with a 2.4 keV thermal temperature and flow standard deviation of just over 150 km/s produces the same peak width as a plasma with no flow variance, but a thermal temperature of 4 keV. On a single line of sight, we have no way to determine whether the width is purely thermal or has instead been augmented by flow effects.

We can repeat the analysis of the (T, u) distribution and associated spectrum for a different line of sight which we call LOS 2 (see again Figure 7 and Figure 8). On LOS 2, we see zero neutron-averaged velocity and only 75 km/s of standard deviation. Consequently, the peak is only slightly upshifted by thermal effect. The width is narrower on LOS 2 than LOS 1 owing to the much smaller σ_v on LOS 2.

We make a key observation when comparing the two lines of sight. While the thermal temperature is the same for both lines of sight – there is, after all, only one plasma producing the neutron signal – the flow variance, σ_v^2 , varies with line of sight due to the low mode asymmetry of the problem. This asymmetry produces peak widths that also vary with line of sight. Interpreting the width as an apparent temperature, we find that T_{Brysk} varies with angle. The angular T_{Brysk} distribution, produced by the constant thermal temperature combined with the varying second moment of the velocity field, must necessarily have a mode 2 distribution, Y_{2m} in spherical harmonics.

Our simulation shows the required mode 2 temperature distribution (see Figure 9). We record the escaping neutron spectrum at 1600 locations evenly distributed, then find the apparent temperature associated with the spectral peak width. This simulated implosion, which has a thermal temperature of 2.2 keV, shows apparent temperatures that range from 2.9 keV to 4.0 keV. The major

axis of the ellipsoidal temperature distribution is aligned with the imposed mode-1 asymmetry. The hot spot flow contains a jet that produces large σ_v in the direction of the imbalance and small σ_v in the plane orthogonal to the imbalance.

Similar temperature variation can, in principle, occur for any asymmetric flow producing a velocity field with a variance that depends on angle. For the purposes of interpreting experimental data we highlight two ideas. First, the lowest observed temperature is closest to the thermal temperature. We cannot know what the true thermal temperature is, but it is certainly no higher than the minimum observation. In our 3D simulation, the lowest possible temperature we could measure (the direction with minimum variance) would be 2.9 keV, a full 700 eV above the thermal temperature, but much closer than the 1.8 keV higher maximum. Second, we emphasize that the difference in temperature with angle is a measure of residual flow asymmetry in the hot spot. Our heavily perturbed 3D simulation has a peak-to-valley variation of 1.1 keV. However, in experiments, we can only measure apparent temperature on lines of sight where we have spectrometers – the 3 nTOFs, the magnetic recoil spectrometer (MRS)^{9,12}, and the neutron imager time-of-flight detector (NITOF). We show in Figure 9 the locations of the diagnostics. At these diagnostic locations, we find a maximum temperature at the specA detector of 3.56 keV and a minimum at the specSP detector of 2.96 keV. The observed peak-to-valley apparent temperature difference is only 600 eV, or 54% of the total variation. In fact, Monte Carlo statistical analysis shows that this diagnostic array captures only about 50 percent of the total temperature variation for most temperature distributions. We should therefore consider measured temperature differences of several hundreds of eV to indicate appreciable flow asymmetry in the neutron-emitting hot spot.

IV. SOME COMPARISONS WITH EXPERIMENTS

Cryogenic, layered DT implosions on the NIF have generated a collection of data against which to compare the expectations we have developed by examining detailed simulated diagnostic output. Some trends in the data match well our new expectations, including X-ray images and differences in neutron-based temperature. In contrast, temperature differences measured using different reactions, DT vs DD, show trends that are at odds with our simulations and theoretical expectations.

A. signatures of implosion asymmetry

We now look at the NIF data from recent layered implosions where high-quality temperature measurements are available from the nTOF detectors. We use the difference in temperature among diagnostic lines of sight to

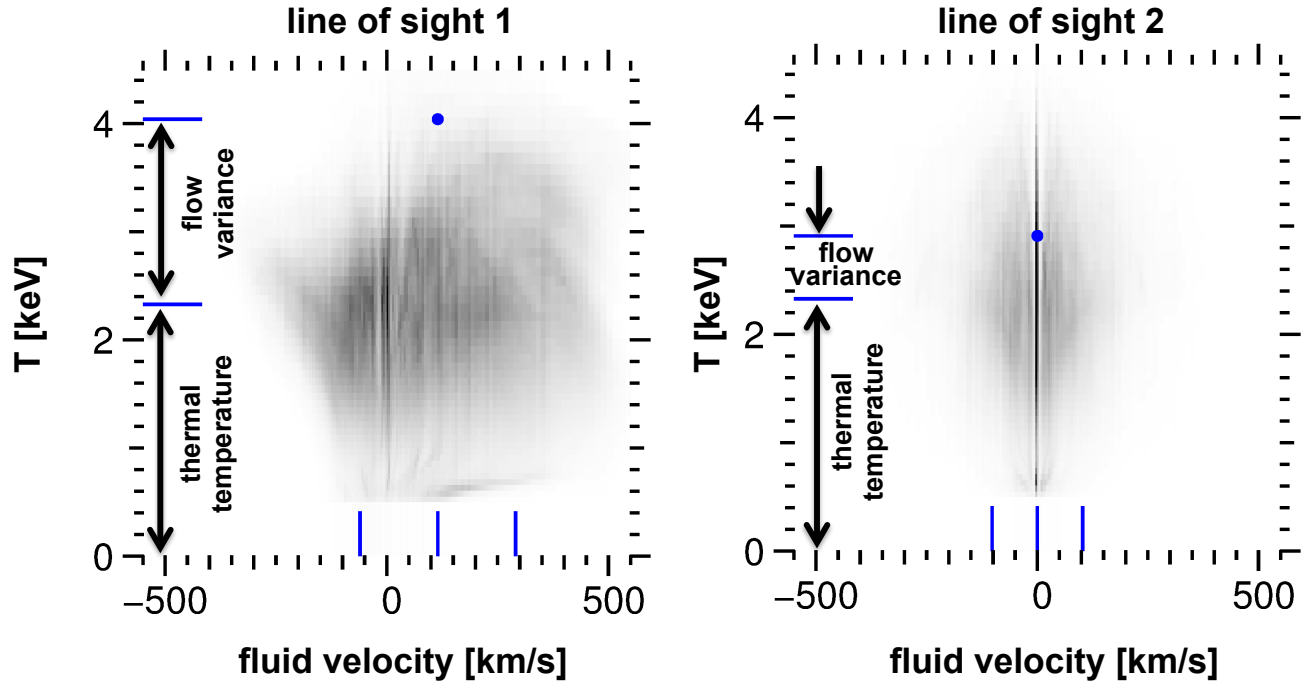


FIG. 7. neutron production distributions in temperature and fluid velocity space, or (T,u) -space, for two lines of sight (LOS). We use the total neutron production at each location in (T,u) -space (temporally and spatially integrated) to illustrate the effects of temperature and flow along a line of sight on the peak features. In each panel, the blue tics on the velocity axis indicate the mean (central tic) and variance of the velocity distribution. The tics on the temperature axis indicate the neutron-averaged thermal temperature (lower tic) and the apparent temperature extracted from the spectral peak width. The blue dot indicates the isolated (T,u) conditions that produce a spectrum indistinguishable from that produced by the distributed (grey scale) source. Importantly, the LOS 1 spectrum has large flow variance that greatly raises the apparent temperature above the thermal. The LOS 2 spectrum has a narrower velocity distribution and a temperature closer to thermal. The difference in apparent temperature from LOS to LOS in a measure of the anisotropy of the underlying flow distribution. The associated spectra are included in Figure 8.

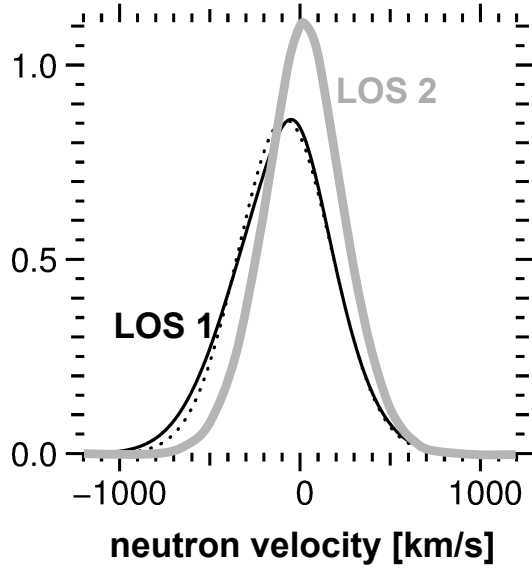


FIG. 8. spectra from the (T,u) distributions in Figure 7. The LOS 1 spectrum is broadened by flow more than the LOS 2 spectrum. The apparent temperature measure in an experiment would be large for LOS 1 than LOS2. For comparison, the dotted spectrum is a symmetric Gaussian. Flow effects have also introduced changes in spectral moments beyond the second, including potentially measurable skewness and kurtosis.

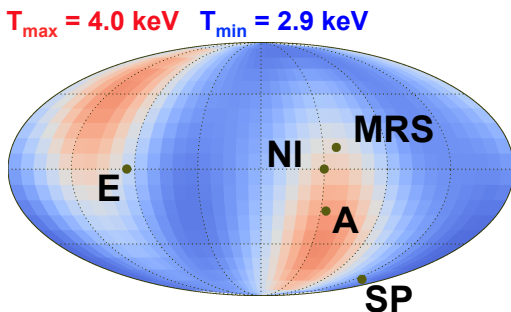


FIG. 9. projection of the spherical map of apparent ion temperature. We compute the apparent temperature (width of the simulated spectral peak) at 1600 locations over the sphere. The map shows the expected $l = 2$ distribution with extremal temperatures of 2.9 keV and 4.0 keV. We also indicate the locations of the 3 nTOF spectrometers (A, E, and SP), the neutron imager time-of-flight spectrometer (NI), and the magnetic recoil spectrometer (MRS). Due to the coverage provided by this array, the spectrometer suite typically captures only half of the total temperature range, in this simulated case 3.0 keV to 3.6 keV.

estimate the residual flow velocity in implosions. Writing equation 2 for the lines of sight with extremal apparent temperature (principle axes of the velocity variance), we find

$$T_{max} = T_{thermal} + \left(\frac{m_D + m_T}{k} \right) \sigma_{v,max}^2 \quad (3)$$

$$T_{min} = T_{thermal} + \left(\frac{m_D + m_T}{k} \right) \sigma_{v,min}^2 \quad (4)$$

$$\sigma_l \equiv \sqrt{\sigma_{v,max}^2 - \sigma_{v,min}^2} = \sqrt{\frac{k(T_{max} - T_{min})}{m_D + m_T}} \quad (5)$$

We derive an lower bound of the residual velocity spread, σ_l , using the observed maximum and minimum temperatures. In Figure 10 we plot σ_l against the maximum temperature difference measured by the detectors ($T_{max} - T_{min}$). The square root relationship of equation 5 is shown in black in the figure. We show in green and in red the results from a slightly asymmetric 2D simulation and the very asymmetric 3D simulation. The blue points are the observed temperature differences for NIF implosions projected onto the black curve. The temperature differences range from 150 to almost 600 eV, suggesting that σ_l ranges from quite small, 70 km/s, to very large, almost 150 km/s. The largest observed temperature differences are similar to our heavily perturbed 3D simulation. Of further interest, we find some correspondence between x-ray image asymmetry and the observed temperature difference. For example, we consider the shot N140311, shown in magenta in Figure 10. This temperature difference indicates a flow asymmetry approaching the levels of the 3D simulation. In Figure 11, we compare the experimental X-ray image from N140311 with the simulated image from our 3D simulation. The simulation was not meant to replicate the conditions of N140311. Nevertheless, the similarity in the x-ray image distortion and the similarity in the neutron temperature asymmetry is encouraging.

B. DD and DT neutron yield trends for further investigation.

We can apply the theory for flow impact on apparent temperature equally well to the neutron peak produced by DT or DD reactions. The only change to equation 2 upon switching reactions is in the total mass of the reactants; for DD we use $(m_D + m_D)$ in place of $(m_D + m_T)$. The mass change alters the weight of the contribution of the non-thermal motion to the width and associated apparent temperature, T_{Brysk} . So, we use equation 3 and equation 4 for both DD and DT to compute the line-of-sight temperature difference $\Delta T = T_{max} - T_{min}$. We find

$$\frac{\Delta T_{DT}}{\Delta T_{DD}} = \frac{T_{max,DT} - T_{min,DT}}{T_{max,DD} - T_{min,DD}} = \frac{m_D + m_T}{m_D + m_D} = \frac{5}{4} \quad (6)$$

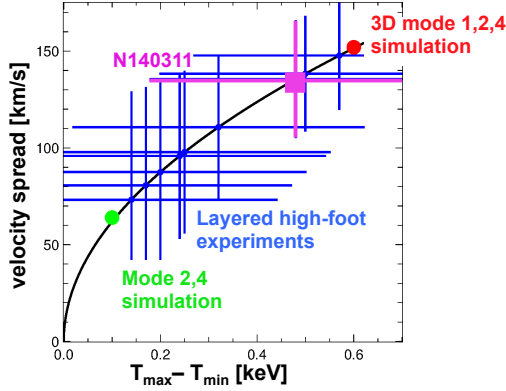


FIG. 10. fluid velocity standard deviation versus apparent temperature difference. We plot the expected trend of velocity spread versus maximum difference between the nTOF apparent temperature measurements. We show in blue the measured temperature differences experimental implosions at NIF. We project the values into velocity spread using equation 5. We highlight the magenta point indicating experiment N140311 (see Figure 11). We also show a lightly perturbed 2D simulated implosion (green) and the heavily perturbed 3D simulation (red). The experiments show a large range of inferred residual hot spot velocity with several experiments approaching 150 km/s.

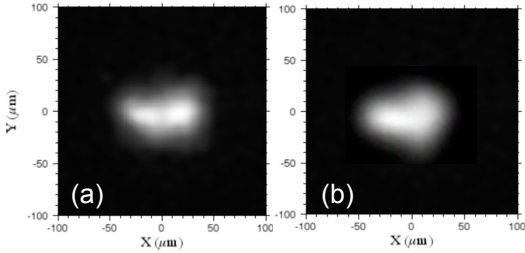


FIG. 11. comparison of experiment N140311 with the 3D simulation. We compare the level of asymmetry seen in the experimental X-ray image (a) with the simulated image (b). While the simulation is not intended to represent exactly the experiment, the degree of asymmetry in the images is similar. Furthermore, the simulated hot spot flow spread lies within the error bar for the experimental inference. See Figure 10.

This simple result suggests we should find temperature variation with line of sight, that is 25% greater for DT than for DD. In fact, we find this ratio for our perturbed 3D simulation to be almost exactly $\frac{5}{4}$ (see Figure 12). However, we also show in Figure 12 the experimental data – it does not agree. The experiments show that the ΔT_{DD} is almost always larger than ΔT_{DT} . Moreover, the experimental DD and DT quantities appear to be independent of one another. This surprising relationship suggests we have more to learn about interpreting the spectral peak properties. We would like to hypothesize that greater scattering by DD neutrons as compared to DT neutrons sets up potential screening issues. We imagine that the heavy scattering of DD neutrons means

that the detected unscattered DD peak neutrons emanate from a more localized (e.g., nearer) region of the hot spot. The lightly scattered DT neutrons, by contrast, issue more nearly from the entire hot spot. This would set up a biasing such that DD and DT neutrons are really sampling different material regions, thereby breaking equation 6 which assumes the neutron signals sample the same flows. Yet, our 3D simulation and associated particle transport package are aware of this very process. Still, the simulation respects equation 6. We have more to learn, and further numerical investigations into the detailed locations of particular particle birth and scattering events for a variety of hot spot and fuel conformations may shed some light.

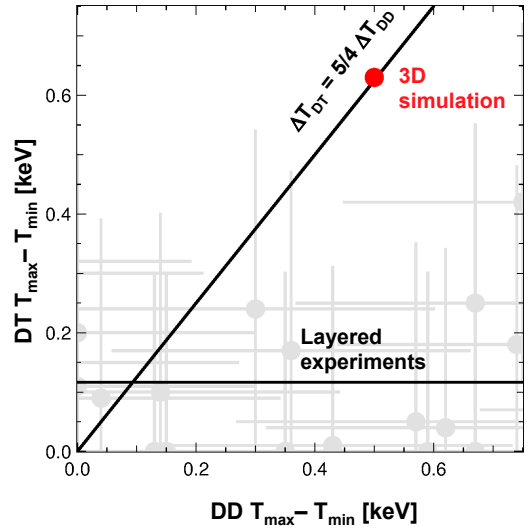


FIG. 12. DD comparison of line-of-sight apparent temperature variation for DD and DT neutrons. We compute the difference between maximum and minimum apparent temperatures for NIF high foot experiments for both DD and DT neutrons (gray points). We show also the expected temperature scaling and the surprising fit to the experimental data. This surprising relationship between DD and DT temperature anisotropy suggests that we are missing ingredients in our understanding of the stagnated fuel assembly.

V. CONCLUSIONS

We have demonstrated a new capability for performing 3D simulations of NIF implosions with multimode drive asymmetry and simultaneous detailed diagnostic output. Our analysis of the simulated diagnostic output for both a particular asymmetric 3D implosion provides some new insight into both X-ray and neutron signatures of asymmetry. We find that highly time- and space-resolved X-ray images, like those provided by NIF's DIXI camera, show hot spot features that have spatial scale lengths in the range of 10 μm and flow features that evolve on time

scales shorter than 30 ps. In contrast to conventional expectations, the X-ray images show little shape variation with X-ray spectral energy. When comparing X-ray images to neutron images, however, we find differences. We attribute these differences to the different emissivities for neutrons and X-rays, as well as the different electron and ion temperatures during the early period of X-ray production. Turning to neutron spectral features, we see that flow in the hot spot, either bulk translation or internal swirling, alters the neutron peak. The bulk translation shifts the center energy of the peak. The hot spot flow velocity variance – swirl, shear, rotation – increases the peak width along a given line of sight. This broadening due to non-thermal motion is indistinguishable from that due to thermal motion. We can examine this broadening, or increase in apparent temperature, from multiple lines of sight to derive a lower bound on the residual velocity variance in the hot spot. We perform this analysis on NIF experimental data. The results show flow velocities ranging from nearly negligible to quite high, with the highest levels being comparable to those seen in our highly perturbed simulation. The implication is that the neutron spectral data support the inference from the X-ray data that the implosions are often appreciably perturbed. Further, the neutron data can provide a quantitative measure of the asymmetry-induced residual flow. Not all data follows our theory and simulations. The most striking discrepancy comes in the relationship between the DT and DD apparent temperature asymmetry. Not only do the temperature asymmetries appear larger in DD than in DT, in direct opposition to our new expectations, but the DD and DT asymmetries appear to be independent of one another. Overall, this exercise has provided us with a better informed set of expectations for experimental data from asymmetric implosions. Some of our new expectations are supported. Some are not, and these provide an opportunity for further insight as we strive to reconcile the discrepancies.

ACKNOWLEDGMENTS

Prepared by LLNL under Contract DE-AC52-07NA27344.

¹Z. A. Ali, V. Yu. Glebov, M. Cruz, T. Duffy, C. Stoeckl, S. Roberts, T. C. Sangster, R. Tommasini, A. Throop, M. Moran, L. Dauffy, and C. Horsefield. Tests and calibration of nif neutron time of flight detectors. *Review of Scientific Instruments*, 79(10), OCT 2008.

²B. Appelbe and J. Chittenden. Relativistically correct DD and DT neutron spectra. *HIGH ENERGY DENSITY PHYSICS*, 11:30–35, JUN 2014.

³L Ballabio, J Kallne, and G Gorini. Relativistic calculation of fusion product spectra for thermonuclear plasmas. *NUCLEAR FUSION*, 38(11):1723–1735, NOV 1998.

⁴H BRYSK. Fusion neutron energies and spectra. *PLASMA PHYSICS AND CONTROLLED FUSION*, 15(7):611–617, 1973.

⁵D. S. Clark, D. E. Hinkel, D. C. Eder, O. S. Jones, S. W. Haan, B. A. Hammel, M. M. Marinak, J. L. Milovich, H. F. Robey, L. J. Suter, and R. P. J. Town. Detailed implosion modeling of

deuterium-tritium layered experiments on the National Ignition Facility. *PHYSICS OF PLASMAS*, 20(5), MAY 2013.

⁶T. R. Dittrich, O. A. Hurricane, D. A. Callahan, E. L. Dewald, T. Doeppner, D. E. Hinkel, L. F. Berzak Hopkins, S. Le Pape, T. Ma, J. L. Milovich, J. C. Moreno, P. K. Patel, H-S Park, B. A. Remington, J. D. Salmonson, and J. L. Kline. Design of a High-Foot High-Adiabat ICF Capsule for the National Ignition Facility. *PHYSICAL REVIEW LETTERS*, 112(5), FEB 5 2014.

⁷James J. Duderstadt and Louis J. Hamilton. *Nuclear Reaction Analysis*. John Wiley and Sons, New York, 1976.

⁸M. J. Edwards, P. K. Patel, J. D. Lindl, L. J. Atherton, S. H. Glenzer, S. W. Haan, J. D. Kilkenny, O. L. Landen, E. I. Moses, A. Nikroo, R. Petrasso, T. C. Sangster, P. T. Springer, S. Batha, R. Benedetti, L. Bernstein, R. Betti, D. L. Bleuel, T. R. Boehly, D. K. Bradley, J. A. Caggiano, D. A. Callahan, P. M. Celliers, C. J. Cerjan, K. C. Chen, D. S. Clark, G. W. Collins, E. L. Dewald, L. Divol, S. Dixit, T. Doeppner, D. H. Edgell, J. E. Fair, M. Farrell, R. J. Fortner, J. Frenje, M. G. Gatu Johnson, E. Giraldez, V. Yu Glebov, G. Grim, B. A. Hammel, A. V. Hamza, D. R. Harding, S. P. Hatchett, N. Hein, H. W. Herrmann, D. Hicks, D. E. Hinkel, M. Hoppe, W. W. Hsing, N. Izumi, B. Jacoby, O. S. Jones, D. Kalantar, R. Kauffman, J. L. Kline, J. P. Knauer, J. A. Koch, B. J. Kozioziemski, G. Kyrala, K. N. LaFortune, S. Le Pape, R. J. Leeper, R. Lerche, T. Ma, B. J. MacGowan, A. J. MacKinnon, A. Macphee, E. R. Mapoles, M. M. Marinak, M. Mauldin, P. W. McKenty, M. Meezan, P. A. Michel, J. Milovich, J. D. Moody, M. Moran, D. H. Munro, C. L. Olson, K. Opachich, A. E. Pak, T. Parham, H. S. Park, J. E. Ralph, S. P. Regan, B. Remington, H. Rinderknecht, H. F. Robey, M. Rosen, S. Ross, J. D. Salmonson, J. Sater, D. H. Schneider, F. H. Seguin, S. M. Sepke, D. A. Shaughnessy, V. A. Smalyuk, B. K. Spears, C. Stoeckl, W. Stoeffl, L. Suter, C. A. Thomas, R. Tommasini, R. P. Town, S. V. Weber, P. J. Wegner, K. Widman, M. Wilke, D. C. Wilson, C. B. Yeamans, and A. Zylstra. Progress towards ignition on the National Ignition Facility. *PHYSICS OF PLASMAS*, 20(7), JUL 2013.

⁹J. A. Frenje, D. T. Casey, C. K. Li, F. H. Seguin, R. D. Petrasso, V. Yu. Glebov, P. B. Radha, T. C. Sangster, D. D. Meyerhofer, S. P. Hatchett, S. W. Haan, C. J. Cerjan, O. L. Landen, K. A. Fletcher, and R. J. Leeper. Probing high areal-density cryogenic deuterium-tritium implosions using downscattered neutron spectra measured by the magnetic recoil spectrometer. *PHYSICS OF PLASMAS*, 17(5), MAY 2010. 51st Annual Meeting of the Division-of-Plasma-Physics of the American-Physics-Society, Atlanta, GA, NOV 02–06, 2009.

¹⁰O. A. Hurricane, D. A. Callahan, D. T. Casey, P. M. Celliers, C. Cerjan, E. L. Dewald, T. R. Dittrich, T. Doeppner, D. E. Hinkel, L. F. Berzak Hopkins, J. L. Kline, S. Le Pape, T. Ma, A. G. MacPhee, J. L. Milovich, A. Pak, H. S. Park, P. K. Patel, B. A. Remington, J. D. Salmonson, P. T. Springer, and R. Tommasini. Fuel gain exceeding unity in an inertially confined fusion implosion. *NATURE*, 506(7488):343+, FEB 20 2014.

¹¹O. A. Hurricane, D. A. Callahan, D. T. Casey, P. M. Celliers, C. Cerjan, E. L. Dewald, T. R. Dittrich, T. Doeppner, D. E. Hinkel, L. F. Berzak Hopkins, J. L. Kline, S. LePape, T. Ma, A. G. MacPhee, J. L. Milovich, A. Pak, H. S. Park, P. K. Patel, B. A. Remington, J. D. Salmonson, P. T. Springer, and R. Tommasini. Corrigendum: Fuel gain exceeding unity in an inertially confined fusion implosion. *Nature*, 510(7505):432–432, 06 2014.

¹²M. Gatu Johnson, D. T. Casey, J. A. Frenje, C-K. Li, F. H. Seguin, R. D. Petrasso, R. Ashabranner, R. Bionta, S. LePape, M. McKernan, A. Mackinnon, J. D. Kilkenny, J. Knauer, and T. C. Sangster. Measurements of collective fuel velocities in deuterium-tritium exploding pusher and cryogenically layered deuterium-tritium implosions on the NIF. *PHYSICS OF PLASMAS*, 20(4), APR 2013.

¹³A. L. Kritcher, R. Town, D. Bradley, D. Clark, B. Spears, O. Jones, S. Haan, P. T. Springer, J. Lindl, R. H. H. Scott, D. Callahan, M. J. Edwards, and O. L. Landen. Metrics for long wavelength asymmetries in inertial confinement fusion im-

- plosions on the National Ignition Facility. *PHYSICS OF PLASMAS*, 21(4), APR 2014.
- ¹⁴G. A. Kyrala, J. L. Kline, S. Dixit, S. Glenzer, D. Kalantar, D. Bradley, N. Izumi, N. Meezan, O. Landen, D. Callahan, S. V. Weber, J. P. Holder, S. Glenn, M. J. Edwards, J. Koch, L. J. Suter, S. W. Haan, R. P. J. Town, P. Michel, O. Jones, S. Langer, J. D. Moody, E. L. Dewald, T. Ma, J. Ralph, A. Hamza, E. Dzenitis, and J. Kilkenny. Symmetry tuning for ignition capsules via the symcap technique. *PHYSICS OF PLASMAS*, 18(5), MAY 2011. 52nd Annual Meeting of the APS Division of Plasma Physics, Chicago, IL, 2010.
- ¹⁵O. L. Landen, J. Edwards, S. W. Haan, H. F. Robey, J. Milovich, B. K. Spears, S. V. Weber, D. S. Clark, J. D. Lindl, B. J. MacGowan, E. I. Moses, J. Atherton, P. A. Amendt, T. R. Boehly, D. K. Bradley, D. G. Braun, D. A. Callahan, P. M. Celliers, G. W. Collins, E. L. Dewald, L. Divol, J. A. Frenje, S. H. Glenzer, A. Hamza, B. A. Hammel, D. G. Hicks, N. Hoffman, N. Izumi, O. S. Jones, J. D. Kilkenny, R. K. Kirkwood, J. L. Kline, G. A. Kyrala, M. M. Marinak, N. Meezan, D. D. Meyerhofer, P. Michel, D. H. Munro, R. E. Olson, A. Nikroo, S. P. Regan, L. J. Suter, C. A. Thomas, and D. C. Wilson. Capsule implosion optimization during the indirect-drive National Ignition Campaign. *PHYSICS OF PLASMAS*, 18(5), MAY 2011.
- ¹⁶MM Marinak, GD Kerbel, NA Gentile, O Jones, D Munro, S Polaine, TR Dittrich, and SW Haan. Three-dimensional hydra simulations of national ignition facility targets. *PHYSICS OF PLASMAS*, 8(5):2275–2280, 2001.
- ¹⁷T. J. Murphy. The effect of turbulent kinetic energy on inferred ion temperature from neutron spectra. *PHYSICS OF PLASMAS*, 21(7), JUL 2014.
- ¹⁸J. L. Peterson, P. Michel, C. A. Thomas, and R. P. J. Town. The impact of laser plasma interactions on three-dimensional drive symmetry in inertial confinement fusion implosions. *PHYSICS OF PLASMAS*, 21(7), JUL 2014.
- ¹⁹Brian K. Spears, M. J. Edwards, S. Hatchett, J. Kilkenny, J. Knauer, A. Kritch, J. Lindl, D. Munro, P. Patel, H. F. Robey, and R. P. J. Town. Mode 1 drive asymmetry in inertial confinement fusion implosions on the national ignition facility. *Physics of Plasmas (1994-present)*, 21(4):–, 2014.
- ²⁰Brian K. Spears, S. Glenzer, M. J. Edwards, S. Brandon, D. Clark, R. Town, C. Cerjan, R. Dylla-Spears, E. Mapoles, D. Munro, J. Salmonson, S. Sepke, S. Weber, S. Hatchett, S. Haan, P. Springer, E. Moses, J. Kline, G. Kyrala, and D. Wilson. Performance metrics for inertial confinement fusion implosions: Aspects of the technical framework for measuring progress in the National Ignition Campaign. *PHYSICS OF PLASMAS*, 19(5), MAY 2012.